The feasibility of high-temperature aquifer thermal energy storage in Denmark: the Gassum Formation in the Stenlille structure

LISA PASQUINELLI, MARITA FELDER, MATS LUNDH GULBRANDSEN, THOMAS MEJER HANSEN, JUN-SEO JEON, NICOLAAS MOLENAAR, KLAUS MOSEGAARD & IDA LYKKE FABRICIUS

Heat storage in the Danish subsurface is gaining increasing interest for optimizing the use of energy resources, but no deep heat storage facilities have yet been established. As an analogue we study the Gassum Formation in the Stenlille structure that is presently used for gas storage. This allows us to discuss geological and technical characteristics of an aquifer relevant for heat storage in Denmark. We develop a 3D model for a high-temperature aquifer thermal energy storage system using analysis of geological core data, sedimentological description, geophysical data including well logs and seismic lines, as well as a finite difference model to calculate the recovery efficiency, heat storage capacity and thermal breakthrough time. Based on geostatistical methods we made three realisations and found similar results for the three cases. In accordance with results from published simplified models we found a high recovery efficiency of 70% after 4 years and 69% after 20 years, a high heat storage capacity of 1.8×10^{18} J, and a long thermal breakthrough time of 66–77 years. These results reflect the excellent reservoir properties of the Gassum Formation in Stenlille, characterised by a uniformly layered sand/shale sedimentology, a high average porosity of 25% and a high permeability of 1000 to 10 000 mD of sandstone intervals.

Keywords: HT-ATES, sedimentary rocks, rock properties modelling, geostatistics, recovery efficiency, storage capacity, thermal breakthrough time.

Lisa Pasquinelli [pasquinellilisa@gmail.com] and Ida Lykke Fabricius [ilfa@byg.dtu. dk], Department of Civil Engineering, DTU BYG, Nordvej Building 119, DK-2800 Kgs. Lyngby, Denmark. Marita Felder [m.felder@panterra.nl], Panterra GeoConsulting,
Weversbaan 1–3, NL-2352 BZ Leiderdorp, the Netherlands. Mats Lundh Gulbrandsen [mats.lundh@nbi.ku.dk], Klaus Mosegaard [mosegaard@nbi.ku.dk], Solid Earth Physics and Computational Geoscience, Niels Bohr Institute, University of Copenhagen, Juliane Maries Vej 30, DK-2100 Copenhagen Ø, Denmark. Thomas Mejer Hansen [tmeha@geo.au.dk], Solid Earth Physics and Computational Geoscience, Niels Bohr Institute, University of Copenhagen, Denmark (Now at: Institute for Geoscience, Høegh-Guldbergs Gade 2, Building 1671, 120, DK-8000 Aarhus C, Denmark). Jun-Seo Jeon, Department of Civil and Environmental Engineering, KAIST, Daejeon, 305–701, South Korea. Nicolaas Molenaar [nicolaasmolenaar@gmail.com], Molenaar GeoConsulting,
Paganinidreef 64, NL-2253 SK Voorschoten, the Netherlands.

Corresponding author: Ida Lykke Fabricius

Heat storage technology could promote the reduction of emission of greenhouse gases and the use of fossil fuel resources because of the possibility to store the excess of energy production from waste incineration, solar panels, biomass plants, industrial processes and wind mills. Among the heat storage technologies, the implementation of High-Temperature Aquifer Thermal Energy Storage (HT-ATES) systems, integrated with existing or new geothermal plants, allows minimal heat loss and large storage capacity. In an aquifer storage system a porous and permeable aquifer is used as storage medium. These storage systems can be classified on the basis of aquifer temperature: low to moderate (10–40°C) or high temperatures (40–150°C) (Lee 2013). Corresponding depth ranges are shallow storage: 10–500 m (Visser *et al.* 2015) and deep storage: 700–2000 m (Sippel *et al.* 2013; Zeghici *et al.* 2015). An ATES system can be considered based on cold injection when the injection temperature is lower than the aquifer temperature (Saeid *et al.* 2013), and hot injection when the injection temperature is higher than the aquifer temperature (Visser *et al.* 2015). The principle of seasonal cycling for an HT-ATES system can be summarized as this: the deep aquifer is penetrated by wells; in winter, cold water from a heat exchanger is injected into the cold wells, while warm water from the aquifer is extracted from the warm wells; in summer the pattern is reversed, and heat is stored in the aquifer by injection of heated formation water of 75–200°C (Pedersen *et al.* 2014). HT-ATES is particularly interesting in Denmark, where several sandstone reservoirs may be suitable for heat storage (Nielsen *et al.* 2004; Mathiesen *et al.* 2013).

Heat storage modelling can be based on an actual case or be based on realistic values for reservoir properties for a non-specific case (Jeon *et al.* 2015; Major *et al.* 2018 and citations therein). In the present study we use geological and geophysical data to model the Gassum Formation of the Stenlille structure as an equivalent for a heat storage facility, although in reality it is a gas storage. The reason for this choice is threefold: 1) The Gassum Formation is a promising target for heat storage in Denmark, 2) No actual HT-ATES system has yet been established in Denmark, 3) The Stenlille structure has been mapped with seismic lines and has been targeted by several logged and cored wells. Because these existing data are used as input for the modelling, the results of the subsequent heat storage modelling cannot be compared to actual data, only to existing simplified models. In Europe, published ATES modelling based on case histories mainly address shallow storage although a few studies include deep storage. Sippel *et al.* (2013) provide a deep 3D thermal model of the Berlin subsurface and Zeghici *et al.* (2015) performed a sensitivity analysis

of the main parameters affecting deep HT-ATES efficiency in the Bucharest region.

Modelling heat storage and transport involves the combination of several parameters: geological reservoir parameters (geological layering and lithology, porosity, thermal properties of rocks, permeability, reservoir depth and temperature) as well as technical parameters of the ATES system (injection temperature, operation time). The reservoir must be permeable, porous and well insulated at the top and base, and it must be continuous over the investigation area. In most cases porosity is estimated from a pre-existing geological model and applied as an average value (Saeid *et al.* 2013; Sippel *et al.* 2013), whereas in some cases porosity estimation is based on well logs (Visser *et al.* 2015). Thermal properties of rocks can be estimated from laboratory testing (Saeid *et al.* 2013) and from average values based on a pre-existing geological model (Sippel *et al.* 2013; Zeghici *et al.* 2015). Visser *et al.* (2015) proposed thermal property estimation from log analysis and an empirical relation with shale volume and porosity. Møller *et al.* (2019) compiled data on thermal conductivity of Danish sediments and rocks. Permeability is typically derived as an average value based on a pre-existing geological model (Sippel *et al.* 2013), although Visser *et al.* (2015) proposed permeability estimation from log analysis and an empirical relation with median grain size, followed by a 3D model for the entire reservoir developed by kriging. Aquifer temperature is estimated from in situ measurements (Saeid *et al.* 2013) or given as an average value based on a pre-existing thermal model (Sippel *et al.* 2013, Zeghici *et al.* 2015).

ATES systems are typically designed for being used for 10–30 years (Saeid *et al.* 2013), but it can be useful to model the performance of the ATES system during the first 1–4 years in order to avoid operational problems like well clogging and formation of bacterial communities (Lerm *et al.* 2013; Visser *et al.* 2015). During injection of hot water, thermal convection and conduction give rise to thermal dispersion along the flow direction, whereas during injection of cold water, convection and conduction give rise to thermal dispersion perpendicular to the flow direction (Saeid *et al.* 2014). In reservoir modelling thermal dispersion is usually included as an average value based on a pre-existing hydrogeological model and well pumping test data (Zeghici *et al.* 2015), but Saeid *et al.* (2014) developed a numerical thermal dispersion model as a function of flow velocity, fluid density, fluid viscosity and fluid temperature.

The aim of this work is to develop a new 3D heat storage model using analyses of geophysical data and core information, and then to calculate the recovery efficiency, lifetime and heat storage capacity of the Gassum Formation in the gas storage facility at Stenlille, Sjælland.

Fig. 1. Map of the Stenlille area on Sjælland with outline of seismic line DN870# 871-001 (shown in Fig. 2) and location of wells (black squares). The blue closed curve outlines the gas-bearing aquifer storage site. The yellow curve is a highway.

The Stenlille structure and facility – geological background

The Stenlille structure is a probably salt-induced NE–SW trending anticlinal structure where sandstone intervals of the Triassic Gassum Formation are deformed to constitute a series of porous and permeable reservoirs sealed by shale and forming traps for injected gas. It is located in the Danish Basin, a WNW–ESE oriented intracratonic basin in the eastern part of the North Sea rift system (Hamberg & Nielsen 2000). The Danish Basin is bounded by the Skagerrak-Kattegat Platform towards the north-east and by the Ringkøbing-Fyn High towards the south-west. According to Vejbæk (1989), the Danish Basin was formed during late Palaeozoic rifting and Mesozoic thermal subsidence along the Skagerrak-Kattegat Platform. Sediment flux from the northern boundary balanced the thermal subsidence, so that the basin remained almost flat with the deepest part in its centre (Hamberg & Nielsen 2000). The Triassic Gassum Formation is widespread in the Danish Basin. It has a variable thickness of 50–150 m and is locally uplifted by salt intrusions as for example in the Stenlille structure. The Stenlille structure is utilized as a gas storage facility by the Danish natural gas project (Laier 2012). It is penetrated by nineteen wells (ST1–ST19 in Fig. 1) and is extensively cored and logged.

The stratigraphic sequence in Stenlille is as follows. Below a less than 100 m thick Quaternary layer, the Chalk Group of Paleocene to Cretaceous age is situated down to around 1250 m; this is underlain by about 300 m shale from the Fjerritslev Formation of Jurassic age, and below a depth of *c.* 1500 m we find the Gassum Formation of Triassic age. The Gassum Formation consists of interbedded shale and sandstones, interpreted as a layer-cake reservoir with laterally continuous (at the scale of the structure) sediment bodies. They were interpreted as sharp-based shoreface sandstones by Hamberg & Nielsen (2000), although this interpretation will be challenged in the present paper.

Based on seismic sections and logging data, the Gassum Formation is divided into three zones (Z1, Z2 and Z3, Figs. 2, 3). The uppermost reservoir interval, Z1, consists of fine- to medium-grained sandstone which can be subdivided into two sandstone units separated by a tight layer with heterolithic facies. The Z2 interval consists of a coarse sandstone succession forming a wedge-shaped body. It is separated from the underlying fine-grained Z3 sandstone unit by another heterolithic interval (Hamberg & Nielsen 2000).
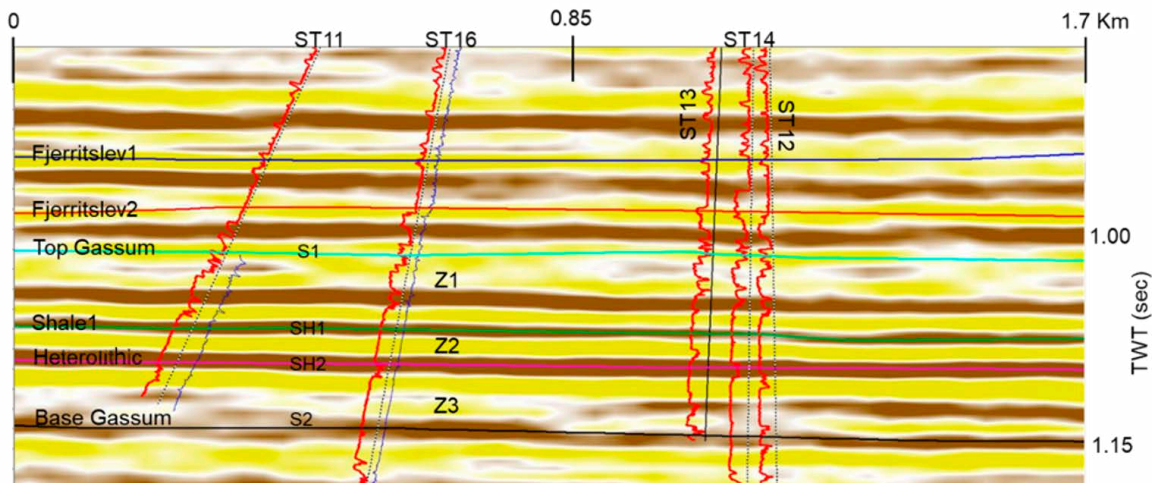
Fig. 2. Part of seismic profile DN 870#871-001 through the central part of the domal structure of Stenlille (Fig. 1). Well logs represented are gamma ray (red) and P-wave velocity (blue). Two reflectors are shown within the Fjerritslev Formation. The reflector S1 represents Top Gassum Formation, whereas reflectors within the Gassum Formation (SH1 and SH2) separate the three reservoir zones (Z1, Z2 and Z3). The reflector S2 represents Base Gassum Formation. Well log traces are linked to the seismic line using a Time Depth chart built in Kingdom – Seismic and Geological Interpretation Software.
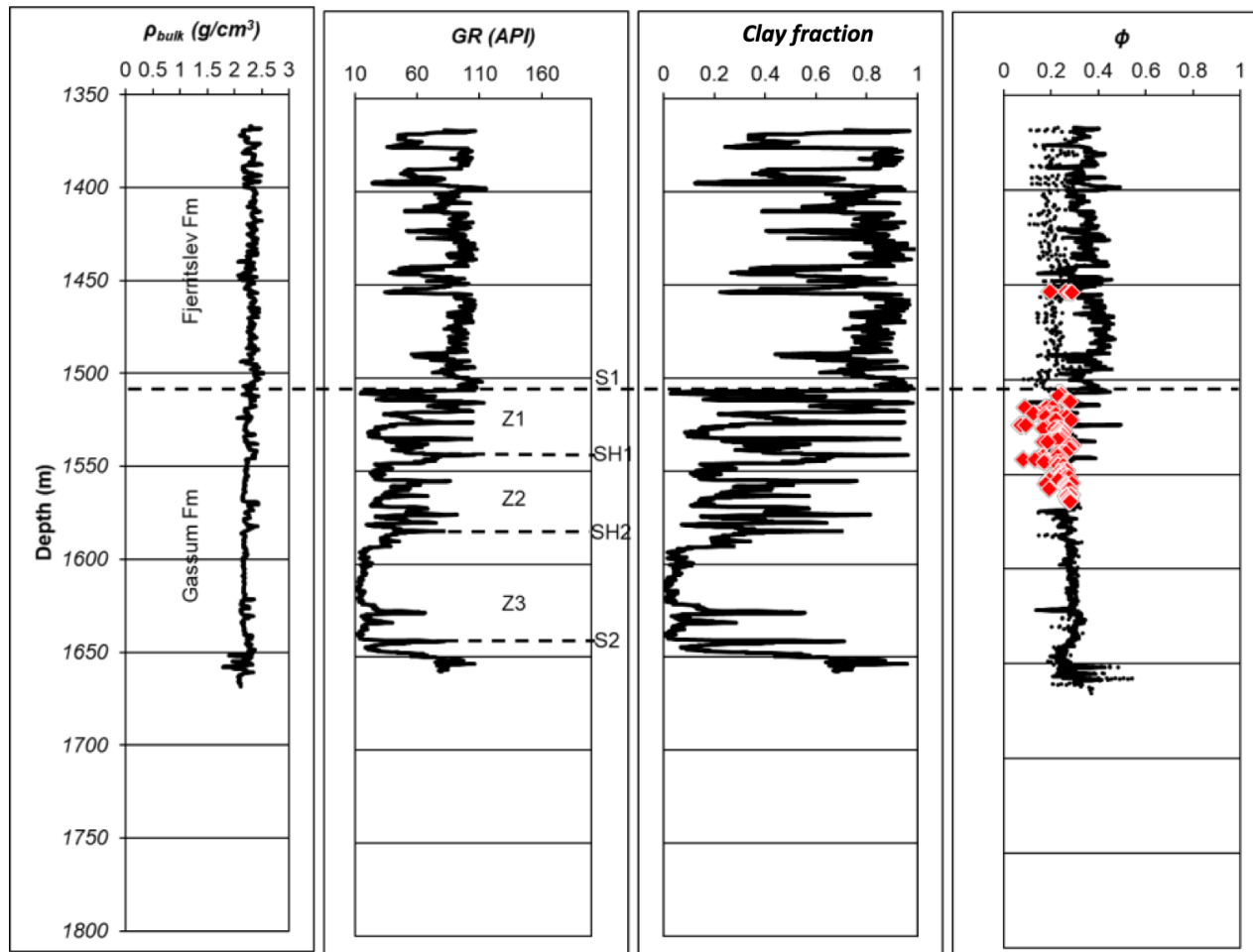

Fig 3. Lithological log interpretation from well ST1 including bulk density (ρ_{bulk}), natural gamma ray (*GR*), clay fraction (V_{cf}), and porosity (ϕ). Neutron porosity is shown as a solid line, density porosity as a dashed line, and core porosity data as red filled diamonds. Depths are with reference to the Kelly Bushing. Z1, Z2 and Z3 represent the three zones of the reservoir between the reflectors S1, SH1, SH2 and S2 (Fig. 2).

Methods

Large amounts of data are available in the form of seismic lines for interpreting the Stenlille structure and well logs to establish stratigraphic correlations and to identify important layers in the Gassum Formation. This allows us to build a consistent geological model and to model petrophysical properties. Drill cores support the interpretation of sedimentary structures and the understanding of palaeogeography and mineralogy of the Gassum Formation, and core tests on thermal conductivity, porosity and permeability can be conducted. These properties are measured by standard core analysis methods, whereas generalisation based on well log analysis mainly is according to standard methods but also includes a recently published method for modelling thermal conductivity (Orlander *et al.* 2018). A geological and geostatistical model of the thermal conductivity and permeability of the Stenlille structure serves as input parameter for numerical simulation. Numerical simulation for recovery efficiency, storage capacity and life time was done with the help of flow and temperature modelling. The wellbore model is approximated as a pile of large voxels (as compared to the borehole radius), so that near-wellbore anomalies (thermal dispersion) contribute only very little to the average energy transport and are not taken into account.

Porosity Modelling

We model porosity from well logging data. In seven wells (ST11, 12, 13, 14, 17, 18 and 19), methane gas is present and a well log interpretation of density and resistivity is done taking the gas into consideration by the following procedure. First, water resistivity R_w is estimated from Archie's equation (Eq. 1 in Archie 1942) assuming that the water saturation S_w is equal to 1.0 in the deepest reservoir zone:

$$S_w{}^2 = \frac{R_w}{\phi^2 R_t} \rightarrow R_w = \phi^2 R_t \,, \tag{1}$$

where R_t is the formation resistivity from the deep resistivity log, and ϕ is porosity estimated from the density log by assuming $S_w =1$, and:

$$\rho_b = (1 - \phi)\rho_0 + \phi S_w \rho_w + \phi(1 - S_w)\rho_g \,, \tag{2}$$

where ρ_b is bulk density from logging data; ρ_0 is mineral density = 2650 kg/m³ (quartz); ρ_w is water density = 1009 kg/m³, and ρ_g is methane density = 173 kg/m³. The fluid densities ρ_w and ρ_g are calculated from PVT equations (citations in Mavko et al. 1998).

The second step is to combine Eq. 1 and Eq. 2 and by iteration find the porosity and water saturation in the gas zone. Archie (1942) multiplied ϕ^2 with a "tortuosity factor", a, but as this concept is not well founded, we assume $a = 1$. In the remaining 12 wells there is no evidence of gas, so $S_w = 1$, and the porosity calculation from density logs is simple (Eq. 2).

Permeability Modelling

We have data for gas permeability (horizontal and vertical), as well as He-porosity, grain density and natural core gamma ray scans in well ST1 from 1507 to 1560 m (Fig. 3), in well ST18 from 1597 to 1672 m, and for three cores in well ST19 from 1630 to 2500 m. When gas is used for measuring permeability, measured values may be greater than the liquid permeability of the rock (Klinkenberg 1941). The effect is significant in sedimentary rocks with low permeability (below 10 mD, Tanikawa & Shimamoto 2009). Core data from the Gassum Formation in Stenlille show high permeability (around 1000–10 000 mD), so we assume that the Klinkenberg effect is small and can be neglected when modelling liquid permeability logs from our laboratory data. We accept that we by this assumption disregard possible turbulence effects.

In order to generate permeability logs, we estimate permeability by using information from core data and well logs. Because permeability of a homogeneous rock with well connected pore space is determined by porosity and specific surface, we use the porosity log and the natural gamma ray log and construct a specific surface log by the following procedure. We first calculate the specific surface (grain surface area per grain volume) from Kozeny's equation for each core sample in well ST19. Kozeny's equation can be written as (Mortensen *et al.* 1998):

$$k = \frac{c\phi^3}{(1-\phi)^2 * S_s^2} = c\,\frac{\phi^3}{S^2} = \frac{c\phi^3 d^2}{(1-\phi)^2 * 6^2} \,, \tag{3}$$

where k is liquid permeability; c is Kozeny's factor (a function of porosity, equation given in Mortensen *et al.* 1998); ϕ is porosity; S_s is specific surface with respect to solid volume; S is specific surface with respect to bulk volume and d is the equivalent grain diameter (Fig. 4A).

From Eq. 3 we calculate S_s:

$$S_s{}^2 = \frac{c\phi^3}{k(1-\phi)^2} \,. \tag{4}$$

The specific surface with respect to the solid mass can be calculated by dividing the specific surface with respect to the solid volume with the grain density of 2.650 kg/m³ for quartz.

We assume that the specific surface (Eq. 4) reflects the clay fraction, V_{cf} of the samples as calculated from the gamma ray index (a simple interpolation between maximum and minimum gamma ray reading); and Mbia *et al.* (2014) found the following relationship between clay fraction and specific surface (Fig. 4B):

$$2 + \log S_s = 2.30\left(V_{cf}\right)^2 + 0.34 V_{cf} - 0.23 \,. \tag{5}$$

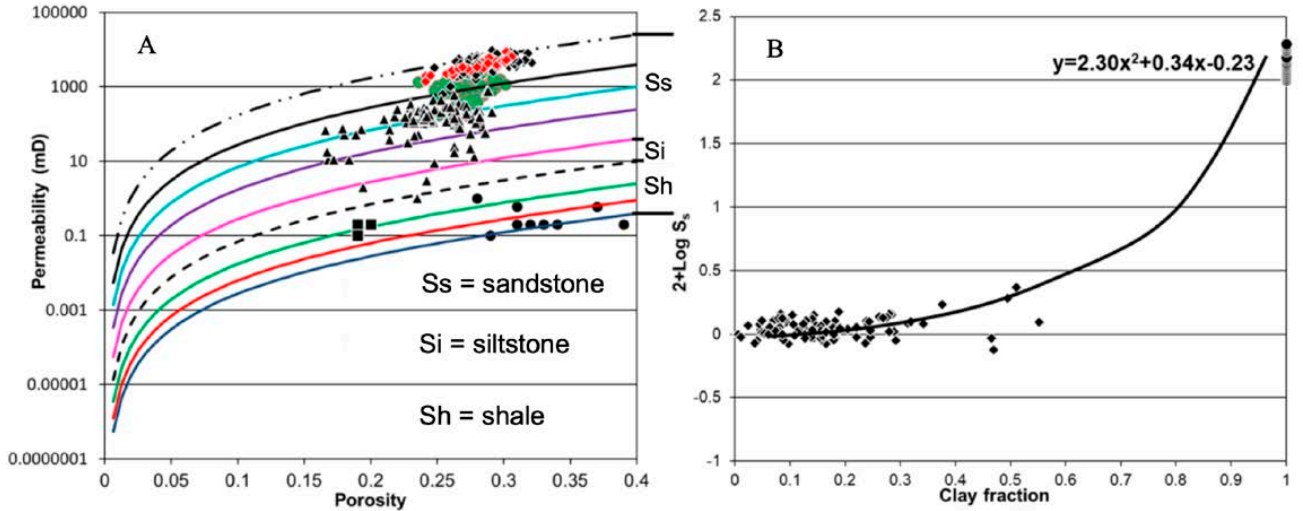Then permeability is calculated using Eq. 3.

Fig. 4. A: Porosity/liquid permeability plot. Distribution of core samples. Coloured lines represent equal grain size curves. Black filled circles are for well ST5, black squares for well ST2 (Mbia *et al.* 2014), black filled triangles for well ST1, green filled circles for well ST18; red and black filled diamonds are for well ST19 and represent respectively horizontal and vertical permeability. **B**: Relationship between clay fraction and volumetric specific surface in well ST19. Values of liquid permeability and specific surface for shales (black filled circles) are taken from Mbia *et al.* (2014). We only have corresponding porosity and clay fraction data for ST19. The black best fit curve is used for modelling permeability.

Thermal Conductivity Modelling

Thermal conductivity is modelled using well log data by first calculating Biot's coefficient, α (Biot 1941) and porosity. Other input parameters are thermal conductivity of minerals and fluids. The obtained thermal conductivity logs are validated by core data and used for reservoir modelling.

Heat transfer in sedimentary rocks with stagnant fluid is governed by the solid contact (Orlander *et al.* 2018). The solid contact is calculated as (1- α). A thermal conductivity model is built for a unit volume of sandstone with porosity ϕ. The unit volume is composed of three parallel heat paths: 1) solid to solid contacts (1- α), 2) free fluid volume β, and 3) a trapped water volume τ (Orlander *et al.* 2018).

In order to find Biot's cefficient, we need to estimate the elastic moduli of dry shale and sandstone from logging data. The bulk modulus K_{fl} of fluid is equal to the bulk modulus of pore water where no gas is indicated by the logs. In gas-bearing intervals we can assume that $K_g = 0.46$ GPa is the bulk modulus for gas calculated from PVT equations, and $K_w = 3.32$ GPa is the bulk modulus for water, based on Mavko *et al.* (1998), so by averaging we get Voigt and Reuss bounds (Mavko *et al.* 1998):

$$K_{flV} = S_w K_w + (1 - S_w)K_g = M_{flV} \qquad (6)$$

$$1/K_{flR} = \frac{S_w}{K_w} + \frac{(1-S_w)}{K_g} = 1/M_{flR} \qquad (7)$$

where K_{flR} is fluid bulk modulus Reuss bound; K_{flV} is fluid bulk modulus Voigt bound; S_w is water satura-

tion calculated from the density and resistivity log, M_{flV} and M_{flR} are Voigt and Reuss bounds for P-wave modulus of the fluid mixture.

We apply Gassmann's fluid substitution equations (Gassmann 1951) approximated in terms of P-wave modulus (Mavko *et al.* 1998) to estimate the P wave modulus M_{dry} in dry conditions. We get

$$\frac{M_{sat}}{M_0 - M_{sat}} \approx \frac{M_{dry}}{M_0 - M_{dry}} + \frac{M_{fl}}{\phi(M_0 - M_{fl})} \text{, where} \qquad (8)$$

$$M_{sat} = \rho_b V_p^2 \qquad (9)$$

is the saturated P-wave modulus where V_p is the P-wave velocity from the acoustic log.

$$A = \frac{M_{sat}}{M_0 - M_{sat}} \text{ , } B = \frac{M_{fl}}{\phi(M_0 - M_{fl})} \qquad (10)$$

$$M_{dry} = \frac{M_0(A-B)}{(A-B+1)} \text{ ,} \qquad (11)$$

where $M_0 = 97$ GPa is the mineral P-wave modulus for quartz, and M_{fl} is the P-wave modulus of the fluid mixture from the average of Voigt and Reuss bounds.

Then Biot's coefficient (α) is approximated by (Fabricius 2014):

$$\alpha \approx 1 - \frac{M_{dry}}{M_0} \qquad (12)$$

Other parameters to be set are the trapped fluid volume τ (Eq. 13), the free fluid volume β (Eq. 14), and the clay volume V_{clay} (Eq. 15).

$$\tau = (1 - c)\phi \qquad (13)$$

$$\beta = c\phi \qquad (14)$$

$$V_{clay} = V_{cf}(1 - \phi) \tag{15}$$

The equations for thermal conductivity, λ, become (Orlander *et al*. 2018):

$$\lambda_{sandstone} = (1-\alpha)\lambda_s + \beta\lambda_{fl} + (\alpha-\beta)^2 \left[\frac{\tau}{\lambda_{fl}} + \frac{V_{clay}}{\lambda_{clay}} + \frac{(\alpha-\phi-V_{clay})}{\lambda_s}\right]^{-1}$$

$$\lambda_{shale} =$$
$$(1-\alpha)\lambda_{clay} + \beta\lambda_{fl} + (\alpha-\beta)^2 \left[\frac{\tau}{\lambda_{fl}} + \frac{(1-\phi-V_{clay})}{\lambda_s} + \frac{(V_{clay}+\alpha-1)}{\lambda_{clay}}\right]^{-1}$$

$$\tag{16}$$

We assume that thermal conductivity of stagnant fluid, λ_{fl}, is 0.62 W m^{-1} K^{-1} for water and 0.025 W m^{-1} K^{-1} for air (Fuchs & Förster 2014), and that the thermal conductivity for minerals is λ_S = 7.7 W m^{-1} K^{-1} for quartz, and λ_{clay} = 6 W m^{-1} K^{-1} for clay minerals. This value for thermal conductivity of clay minerals may seem high, but because clay minerals are too small to allow measurement, the value was estimated from rock physical modelling of data for unconsolidated clay given in Brigaud & Vasseur (1989) (Orlander *et al*. 2018). Please observe that Brigaud & Vasseur (1989) report thermal conductivity of clay–water–air mixtures and not of clay minerals, so the resulting thermal conductivity of the clay mineral depends on the choice of model. Their data would not be in contradiction of a clay mineral conductivity as low as 4 W m^{-1} K^{-1}, but 6 W m^{-1} K^{-1} is an unbiased estimate. In accordance with Orlander *et al*. (2018) we use petrographic evidence (Mbia *et al*. 2014) to model thermal conductivity of the sedimentary rocks by assuming clay as the load-bearing mineral in sections with $V_{cf} = V_{clay}/(1-\phi) > 0.2$, where V_{clay} is clay volume per bulk volume. In sections with $V_{cf} = V_{clay}/(1-\phi) <$ 0.2 we assume quartz to be load-bearing. In general, the depth section from 1250 to 1600 m is identified as clay-supported and the section from 1600 to 1700 m as quartz-supported. In the clay-supported section, modelled values of thermal conductivity range from 2 to 3 W m^{-1} K^{-1} in the saturated case showing good agreement with experimental results by Brigaud & Vasseur (1989) on natural clays. For dry core, modelled thermal conductivity was found to compare well with measured core data from the ST18 well: 106 points were collected using a heat transfer analyzer (Applied Precision Ltd. 2015; Orlander *et al*. 2018). The resulting model will be the input for the flow and temperature model.

Heat Capacity Modelling

Heat capacity is modelled from porosity, bulk density, solid and fluid density, and solid and fluid heat capacity. In a two-component system (rock and water), volumetric heat capacity C_{wet} becomes (Schärli & Rybach 2001):

$$C_{wet} = c_{solid}\rho_0(1 - \phi) + c_w\rho_w\phi \,, \tag{17}$$

where c_w is the specific heat capacity of water and c_{solid} is the specific heat capacity of the solid part of a rock. Heat capacity of the solid should be calculated by taking into account the mineralogical composition of the Gassum Formation (Robertson 1988; Rosenbrand *et al*. 2014):

$$c_{solid}\,\rho_0 = \sum_{i=1}^{N} n_i\rho_i c_i \tag{18}$$

Where n_i is the volume fraction of the i-th mineral, ρ_i is mineral density, and c_i is the specific heat capacity of the i-th mineral (Table 1).

Table 1. Minerals in sandstones and shales in core samples from Stenlille-18

	Sandstones	Specific heat capacity	Volumetric heat capacity
Mineral	n_i (%)	c_i (J kg^{-1} K^{-1})	C_i (MJ m^{-3} K^{-1})
Quartz	72	740	1.96
K feldspar	7.4	628	1.645
Kaolin	6.2	974	2.56
Illite	5.3	800	
Mix clays	4.5	700	
Albite	2.4		
	Shales		
Mineral	n_i (%)	c_i (J kg^{-1} K^{-1})	C_i (MJ m^{-3} K^{-1})
Quartz	42	740	1.96
Kaolin	25	974	2.56
Illite	24	800	
Mix clays	8	700	

Mineral content *(n)* for sandstones (Rosenbrand *et al*. 2014a, b) and shales in ST 18 well (Mbia *et al*. 2014), specific heat capacity with respect the mass (Robertson 1988) and volumetric heat capacity (Poulsen *et al*. 2015) of rock forming minerals.

The geological model of the Stenlille structure

The geological model of the Stenlille structure is made with Petrel 2015 (Petrel 2015). The input data for our model are: Well header (well name, x-y coordinates, datum, true depth), deviation survey (measured depth, dip, azimuth), top of the sandstone zones in well logs (Fig. 3), top of the sandstone zones in seismic lines (Fig. 2). The four interfaces S1, SH1, SH2 and S2 (Fig. 2) are input data for building geological surfaces in Petrel.

Time–depth conversion

The time–depth conversion is done using an attribute guided interpolation technique called Smart Interpretation (SI) (Gulbrandsen *et al*. 2017). This method is mainly built up by two steps. In the first step a statistical relation between a set of observations (e.g. depth to a subsurface layer) and a set of attributes (e.g. travel times) is inferred. In the second step this relation is applied to a new set of the same attributes to perform a prediction (or interpolation/extrapolation)

of the observations (depths) wherever the attributes are available.

In this study the observations are represented by depths in metres to the four subsurface boundaries obtained from the 19 different boreholes, and the attributes guiding the interpolation are four two-way travel time (TWT) maps. These maps are obtained using a combination of manual travel time picking and application of universal kriging. Firstly, the travel times to the four distinct reflectors (representing the subsurface interfaces S1, SH1, SH2 and S2) are picked from the available reflection seismic lines (Fig. 2). Then universal kriging with a second-order polynomial trend model is performed to obtain the TWT maps of the four subsurface layers everywhere in the reservoir. Having obtained the TWT maps, the SI method is used to learn the relation between the depths in TWT and the corresponding depths in metres, locally observed in boreholes, and in turn to estimate the depths (in metres) of the subsurface interfaces S1, SH1, SH2 and S2 throughout the reservoir.

The 3D geological model
For a reservoir simulation model, a discretized representation of the field is necessary, and the space occupied by the rock volume is divided into cells where the structure of the formation is defined by surfaces, and the rock properties are determined from well logs and cores. X and Y increments were chosen to be 10 m, with a Z increment of 5 m in Z1 (the zone between S1 and SH1), 2.5 m in Z2 (the zone between SH1 and SH2), and 5 m in Z3 (the zone between SH2 and S2).

Well log upscaling and the petrophysical model
We first model porosity, clay fraction, thermal conductivity and permeability through upscaling the well log data. For each grid cell, all log values that fall within the cell are averaged (arithmetic mean) to produce one log value for each property in that cell. All other cells have an undefined value. Petrophysical modelling is then done by interpolation or simulation of continuous data throughout the model grid.

We produce three different spatial realisations of each property; each realisation represents an equally probable representation of the spatial distribution of a specific attribute, in our case porosity, permeability, sandstone/clay intervals and thermal conductivity.

Stochastic methods are used to set up variograms for each zone of the 3D model. We use spherical variograms with normal transformation using the gaussian sequential algorithm, a stochastic method for interpolation based on kriging. It can honour input data, input distributions, variograms and trends. To set the range of the variogram, the minor direction is set in the SW–NE direction of the Stenlille structure (Fig.

1), the major direction is set in the NW–SE direction, and the vertical direction is set up at the minimum sandstone thickness that we can detect (2.5 m). The number of lags is limited by the range in which data pairs are well correlated. Then variograms for each zone of the geological model can be implemented together to generate the realisations of porosity, clay fraction, permeability and thermal conductivity. Permeability and thermal conductivity are modelled using co-simulation honouring the clay fraction.

Flow and temperature modelling of the Stenlille structure
The pressure development in space and time is described by the equation:

$$c_t \phi \rho_w \frac{\partial p}{\partial t} - \nabla \cdot \left(\frac{\rho k}{\mu} (\nabla p - g \rho_w \nabla z) \right) = \rho_w q \qquad (19)$$

where p is the pressure, z is depth, t is time, g is the gravity, c_t is the total compressibility (inverse of drained bulk modulus) and q is the outflow (positive or negative) of fluid per volume (see e.g. Peaceman 1991). A rough estimate (Lee 1982, equation 1.47) of the stabilisation time as a function of distance from the injection well (the time required for a pressure transient to reach a given distance) yields a value less than 10 hours for a distance of 100 m. Hence, the stabilisation time is much smaller than our injection period (3 months), even for distances well beyond the maximum radius of the hot water front obtained in our simulations. We therefore conclude that the pressure transient gradient is insignificant for our study and assume that $\partial p / \partial t \approx 0$.

Heat storage simulation is done by combining the flow equation (Eq. 19) with the heat transport equation:

$$\frac{\partial T}{\partial t} = D \nabla^2 T + k \nabla p \cdot \nabla T \qquad (20)$$

(see e.g. Turcotte & Schubert 2014), where T is the temperature, $k \nabla p$ is a flux term, $k \nabla p \nabla T$ is a source term, and D is the thermal diffusivity

$$D = \frac{\lambda_{wet}}{C_{wet}}. \qquad (21)$$

Here, λ_{wet} is the thermal conductivity of rocks in water-saturated condition. Injection/production of hot water at the well site location is set as boundary conditions when solving equations (19) and (20).

Equation (19) is solved numerically by a state-of-the-art finite-element method (Lie *et al*. 2012; Lie 2015). Recent implementations of solutions to equation (20) exist (see e.g. Krogstad *et al*. 2015), and are quite straightforward, but not available in public domain. We therefore developed a 3D finite-difference algorithm for simulation of single-phase, compressible

flow to account for thermal effects, including buoyancy due to temperature variations in the fluid. The algorithm was successfully tested on analytical and semi-analytical benchmark examples of flow in homogeneous reservoirs involving one and two wells. For this modelling, porosity was assumed constant due to its low variability, so inputs are geostatistically simulated permeability and thermal conductivity in water saturated conditions.

We simulate 90 days of injection in the reservoir with a water temperature of 90°C, then 90 days of storage or inactivity of the system, and finally 90 days of production from the reservoir and again 90 days of a second storage. This cycle is repeated 4 and 20 times to simulate 4 to 20 years of injection – production. By assuming a surface temperature of 8°C and a geothermal gradient of 30°/km, the aquifer temperature is set to 55°C in accordance with a personal communication from Hans Øbro. Parameters used to implement the heat transfer model are shown in Table 2.

The most important result obtained from the heat storage modelling is the recovery efficiency defined as the ratio between the recovered energy and the stored energy when the amount of injected and extracted water is the same (Schout *et al.* 2014). Schout *et al.* (2014) calculate the recovery efficiency, ε, based on the produced water temperature, T_p:

$$\varepsilon = \frac{V_p C_w (T_p - T_a)}{V_i C_w (T_i - T_a)} = \frac{T_p - T_a}{T_i - T_a} , \qquad (22)$$

Where T_a is the aquifer temperature and T_i is the injection temperature. V_p and V_i are the produced water volume and the injected water volume, respectively.

A second important result is the storage capacity, Q_s. This is defined as the amount of heat that can be stored in the reservoir (Ataer 2006), given by:

$$Q_s = V_{reservoir} C_{reservoir} \Delta T . \qquad (23)$$

$V_{reservoir}$ is reservoir volume, $C_{reservoir}$ is heat capacity of the reservoir, and ΔT is the maximum temperature difference between injection water and reservoir. This expression can be used to calculate the volume of the reservoir required to store a given quantity of energy. Alternatively, the modelling can provide exergy, defined as the amount of energy that can be extracted (Kupfersberger 2009).

A third important aspect controlling the feasibility of an ATES system is thermal breakthrough, defined as the time when the injected water reaches the production well and the ATES system can be considered finished, meaning that the system is no longer providing the desired energy. Thermal breakthrough time is calculated considering well spacing and water front velocity extrapolated from temperature development at the fourth cycle:

$$t_{breakthrough} = \frac{well\ spacing}{water\ front\ velocity} . \qquad (24)$$

Table 2. Gassum Formation geophysical input parameters

Parameters	Name	Stenlille model	Reference
Horizontal permeability sandstones	k	From geostatistics	Core data
Vertical permeability sandstones	k	From geostatistics	Core data
Thickness of sandstones	$H_{aquifer}$		Logging data
Porosity of sandstones	ϕ	From geostatistics	Logging data
Aquifer Temperature	$T_{aquifer}$	55 °C	
Horizontal permeability for shales	k	From geostatistics	Mbia *et al.* 2014
Vertical permeability for shales	k	From geostatistics	Mbia *et al.* 2014
Thickness of shales	$H_{aquitard}$		Logging data
Shale porosity	ϕ	0.25	Logging data
Surface pressure	p	1 atm	
Flow rate	q	100 m³/day	
Thermal Conductivity sandstones	$\lambda_{-sandstone.}$	From geostatistics	
Volumetric Heat Capacity sandstones	C_{wet}	3 MJ m⁻³ K⁻¹	
Thermal Conductivity shales	λ_{shale}	From geostatistics	
Volumetric Heat Capacity shales	C_{wet}	2 MJ m⁻³ K⁻¹	
Well Spacing	*Well spacing*	1000 m	
Injection Temperature	$T_{injection}$	90 °C	
Days of injection-storage- production		(90-90-90) 4 times	

Results

Core descriptions in Stenlille

Sedimentological descriptions of Stenlille cores and analysis of well logs (Fig. 5) have led to a revised understanding of sedimentological features and an updated geological model of the Gassum Formation in Stenlille.

After the study of wells in the central (ST1, 2, 5, 7, 8, 9, 11, 12, 13, 14, 16, 17, 18 and19) and peripheral parts (ST4, 6, 10 and 15) of the Stenlille structure, we can describe it as a domal structure but with little relief. The Gassum Formation in Stenlille is sedimentologically uniform and is very different from the Gassum Formation as reported in northern Jylland (Hamberg & Nielsen 2000; Nielsen 2003). It has a different composition, sedimentary structures and depositional environment. The three zones of the Gassum Formation are each built by several smaller amalgamated lensoid sandstone bodies that together constitute a sheet (sheet-like beds). The sandstone bodies had a positive morphology above the sea floor and are elongated along a SW–NE axis. The sandstone bodies are clearly separated by heterolithic layers (offshore interbars) and pinch out in all directions (Fig. 6).

The palaeogeographic layout during the deposition of the Gassum Formation, as given by Ziegler (2005), indicate that the coast was located in Skåne and the sandstone bodies, probably storm-built, were detached from the coastline. River input was probably from the south-east, from the Polish Basin. The Fennoscandian High, north of the Danish Basin, probably delivered only little clastic material, because during the deposition of the Gassum Formation there was a large fluvial system between the Fennoscandian High and the Bohemian Massif in Poland (Ziegler 2005) (Fig. 6).

The sandstones of the Gassum Formation are dominated by quartz (Fig. 7). In a sample from the uppermost reservoir interval (Z1), we find quartz grains with dominantly interparticle pores (few oversized secondary pores), and one microcline feldspar in the centre (Fig. 7A). In a sample from the middle reservoir interval (Z2), the dominant phase is quartz with interparticle pores and some secondary oversized pores (Fig. 7B). In plane polarised light a black substance is visible; it may be drilling mud that penetrates throughout the cores because of the high permeability.

Porosity model

Examples of modelled porosities are shown in Fig. 8. The Fjerritslev Formation shows porosities roughly around 0.2, and the Gassum Formation shows ranges between 0.2 and 0.3 (volume fraction).

Permeability model

Examples of modelled permeability are shown in Fig. 9. Permeability ranges from 1000 mD to 10 000 mD for sandstones in the Gassum Formation and from 0.01 mD to 1 mD for shales in the Fjerritslev Formation.

Thermal properties model

Examples of modelled thermal conductivity and modelled heat capacity are shown in Fig. 10 and Fig. 11. In sandstones of the Gassum Formation values for thermal conductivity are between 3 and 4 W m^{-1} K^{-1} and the volumetric heat capacity values are between 2 and 2.5 MJ m^{-3} K^{-1}. In shales of the Fjerritslev Formation the thermal conductivity is between 2 and 3 W m^{-1} K^{-1} and values for volumetric heat capacity are between 2 and 2.5 MJ m^{-3} K^{-1}.

The 3D geological model of the Stenlille structure

As a main result from the 3D model of the Stenlille structure, a contour map of each of the four surfaces is generated (Fig. 12), and as another main result from the 3D geostatistical model of the Stenlille structure, three different but statistically equally possible outcomes (realisations) are modelled for the rock properties (clay fraction, thermal conductivity, Fig. 13). The realisations illustrate the uncertainty/variability of the clay fraction and thermal conductivity in the Stenlille reservoir due to uncertainties/variability in seismic data and rock physical parameters. Poorly constrained properties (typically small-scale features) of the models show high variability and are therefore uncertain, whereas well-constrained properties (typically large-scale features) are less variable and therefore less uncertain.

The flow and temperature modelling of the Stenlille structure

Figure 14A–C shows the temperature development after injection of hot water (90°C) after 3 years and 90 days (after the fourth cycle) in horizontal section for three realisations of the Stenlille reservoir. Figure 14D–F shows the temperature development after production after 3 years and 270 days for the three realisations of the Stenlille reservoir.

▶ **Fig. 5.** Core description of ST14. It is composed of ten columns representing, from left to right: measured depth (MD); the gamma ray log (GR); stratigraphy of the well (blue is the Fjerritslev Formation and yellow is the Gassum Formation); position of the four cores studied; measured porosity in cores; permeability (gas permeability was assumed roughly equal to liquid permeability); lithology; grain size and sedimentary structures; the seismic units Z1 to Z3 identified on the seismic line in Fig. 2; and sedimentary environment. Depth reference is to the Kelly Bushing; and ST14 is a deviated well, so that depths are *c.* 100 m deeper than true depth.
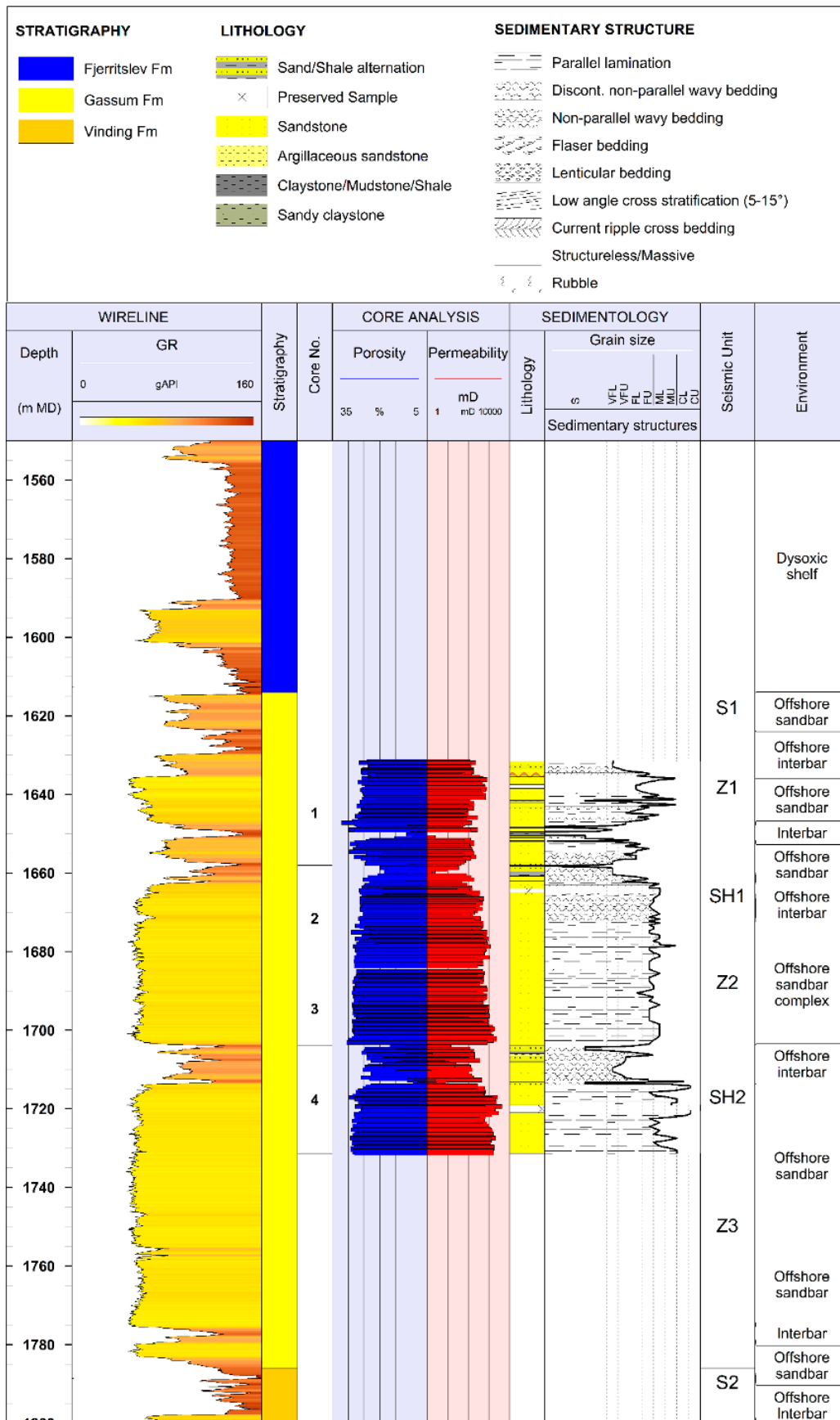
Figure 15A–C shows the temperature development after injection of hot water (90°C) after 3 years and 90 days (after the fourth cycle) in vertical section for three realisations of the Stenlille reservoir, and Figs 15D–F shows the temperature development after production after 3 years and 270 days for the three realisation of the Stenlille reservoir in vertical section.

Recovery efficiency, thermal breakthrough time and storage capacity are shown in Tables 3 and 4. Thermal breakthrough time is calculated from Eq. 24 at the fourth cycle of simulation. Estimating a water front velocity of 15 m/year and a well spacing of 1000 m, thermal breakthrough time is 66 years, equal to 16 cycles of four years each. In order to validate the model,
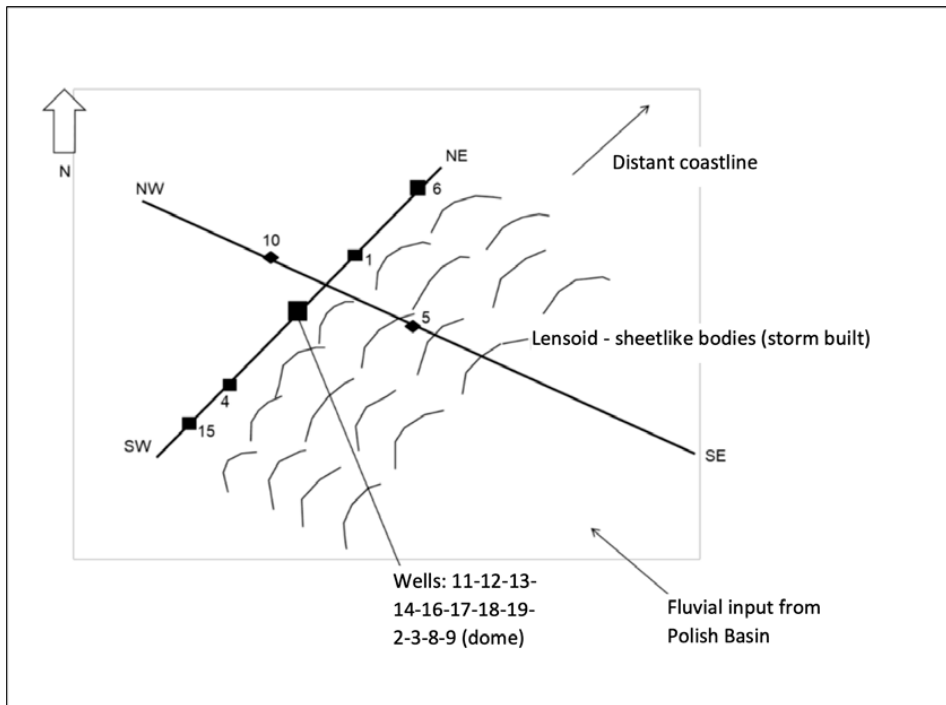
Fig. 6. Palaeogeographic concept of the Gassum Formation at Stenlille. Black filled squares and diamonds are location of wells. The two black lines indicate the location of seismic lines. Squares represent wells aligned on the major axis of Stenlille structure, diamonds represent wells aligned on the minor axis of the Stenlille structure.
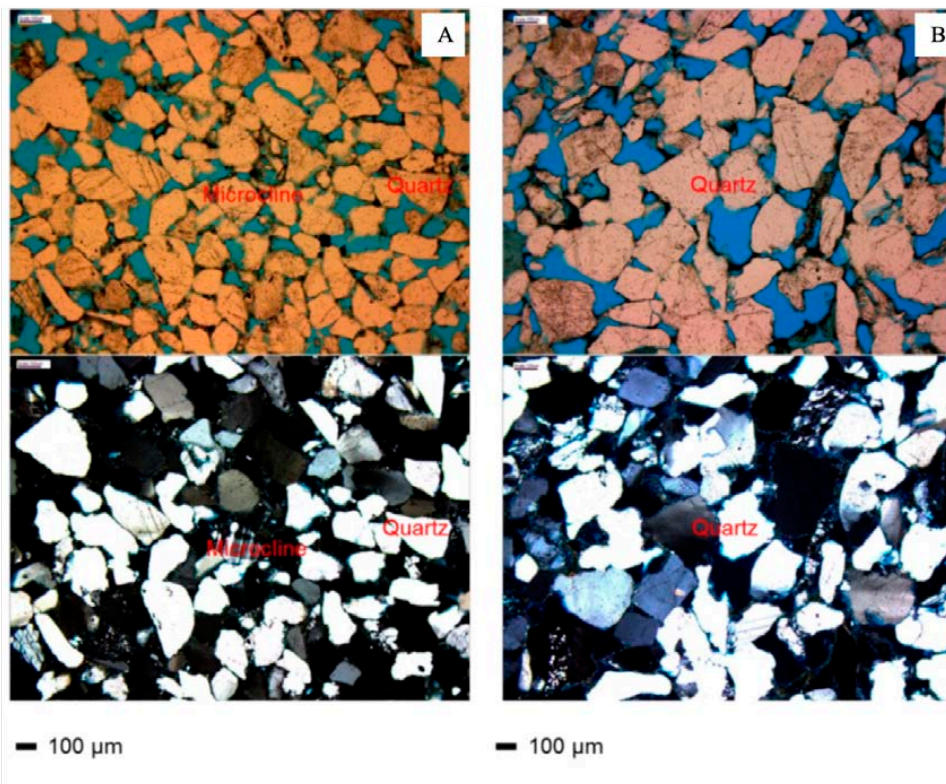
Fig. 7. Thin section micrographs. **A**: Well ST14 at 1638 m, plane-polarised light (above) and crossed nicols (below), zone Z1. **B**: Well ST14 at 1683 m, plane-polarised light (above) and crossed nicols (below), zone Z2. Total width of images 2160 μm. Pore space is blue in plane-polarised light and black under crossed nicols.
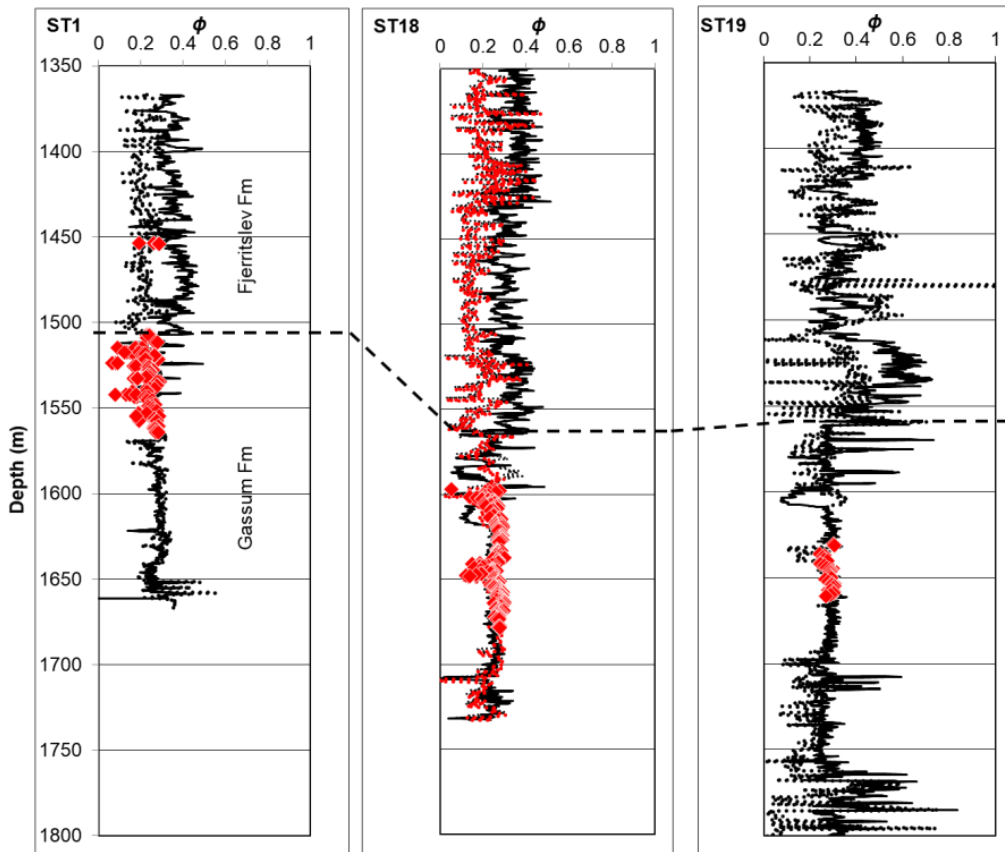
Fig. 8. Porosities for wells ST1, 18 and 19. Black continuous lines represent neutron porosity, black dashed lines represent density porosity. Red squares represent core data. The red dashed line for ST18 is the gas-corrected porosity. For ST1 and ST19 the core porosity is equal to the density porosity. Depths are MD (measured depth).
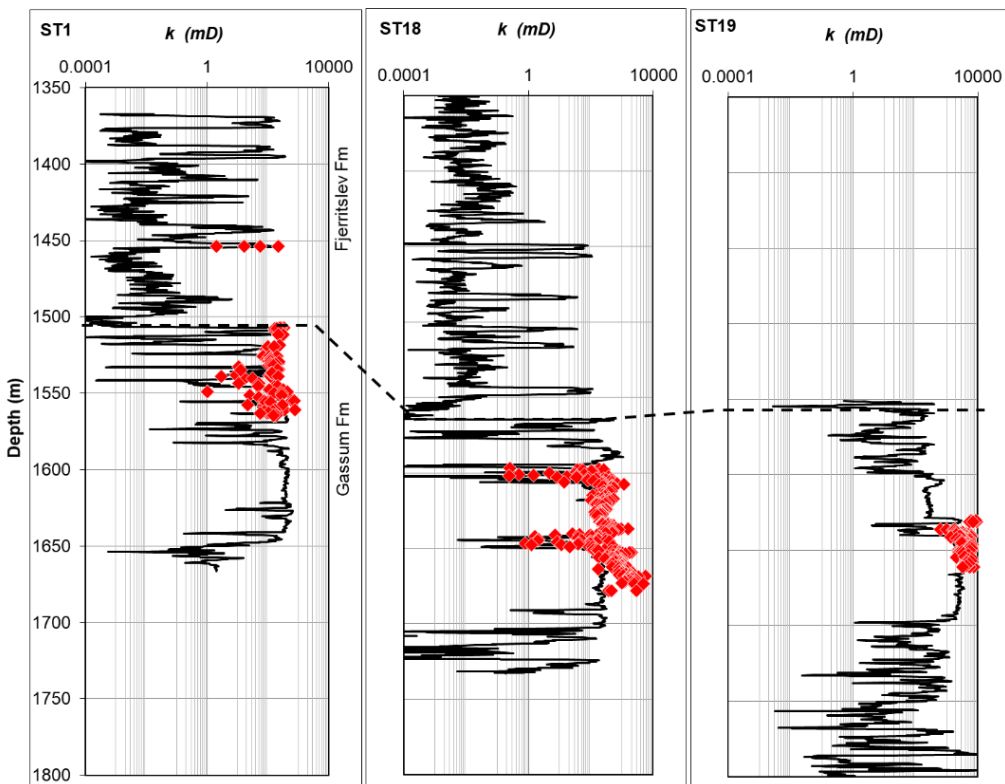

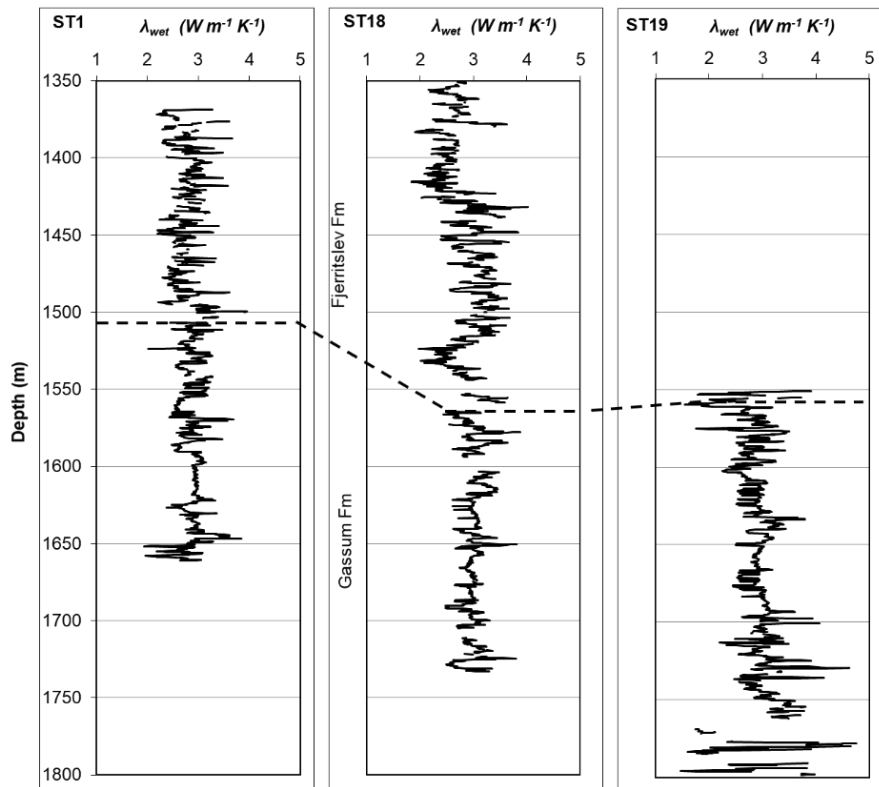**Fig. 9.** Modelled liquid permeability logs for wells ST1, 18 and 19. Red squares represent gas permeability core data. Depths are MD (measured depth).

Fig. 10. Modelled thermal conductivity at saturated conditions for wells ST1, 18 and 19. Depths are MD (measured depth).
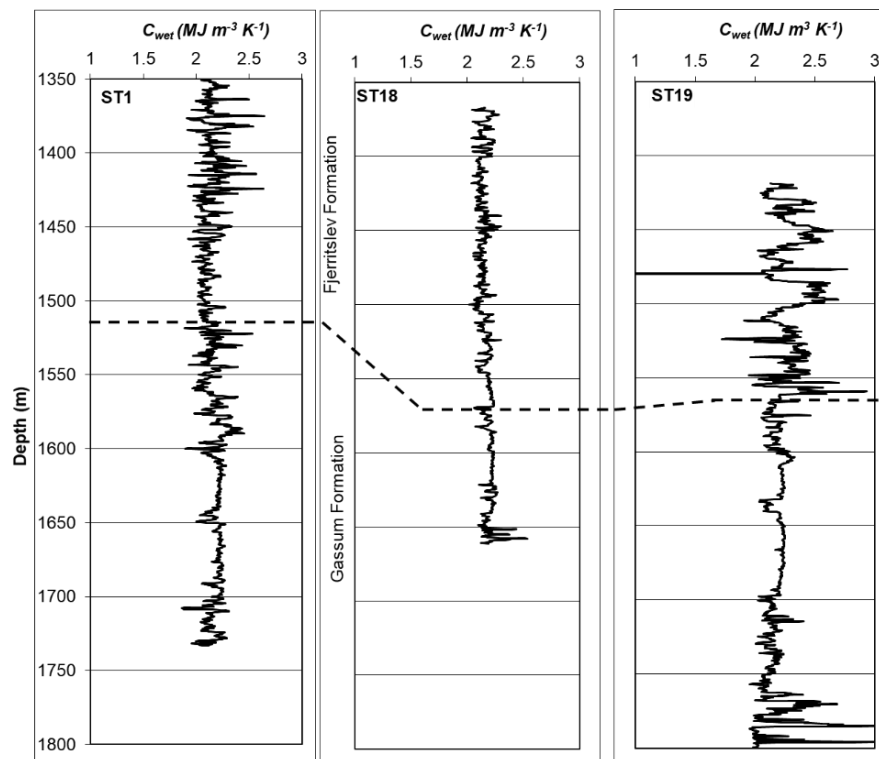
Fig. 11. Modelled volumetric heat capacity in wet conditions (C_{wet}) for wells ST1, 18 and 19. The heat capacity of quartz (1.96 MJ m^{-3} K^{-1}) is used for the model. Depths are MD (measured depth).
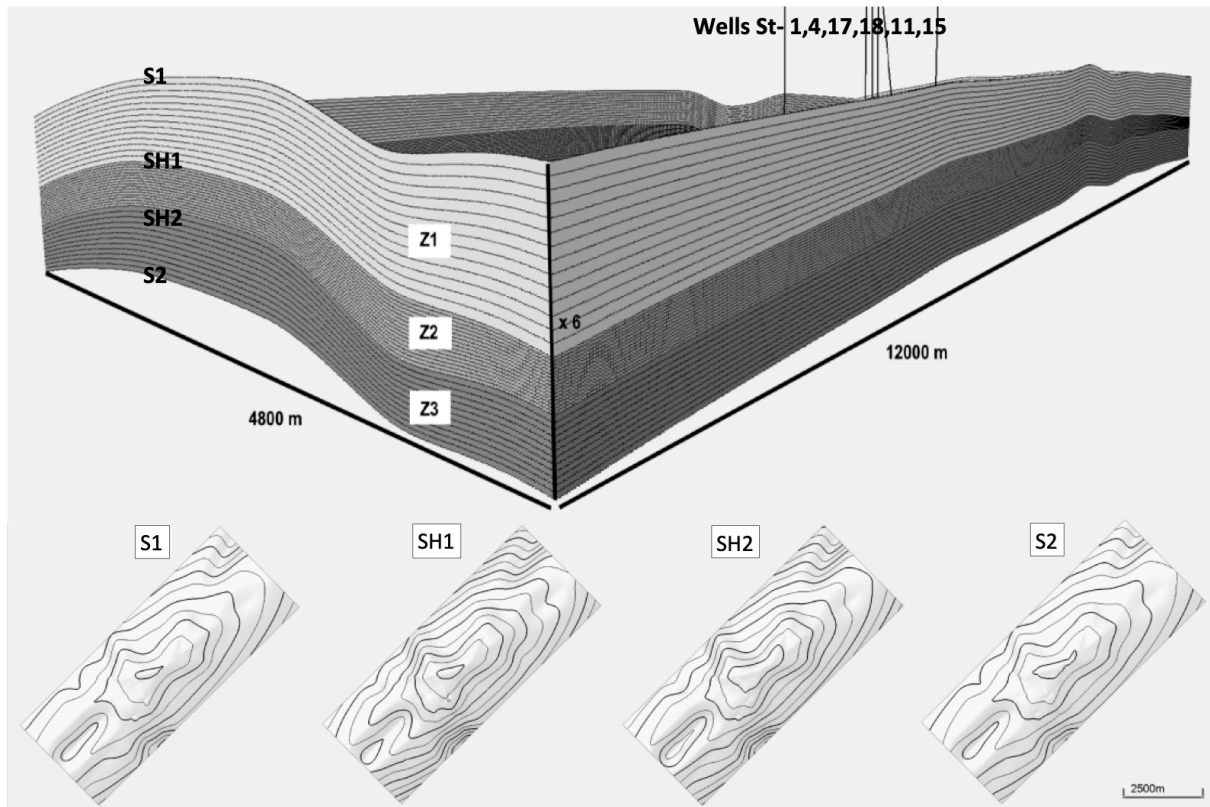
Fig. 12. Perspective view of a 3D model of the three zones, Z1, Z2 and Z3, in the Gassum Formation. The model is also presented as four contour maps of the SW–NE trending domal structure, from left: top Gassum Formation (S1), top shale member (SH1), top main heterolithic interval (SH2), and base Gassum Formation (S2). Contour interval 10 m. The top contour of the S1 map is -1460 m, the top contour of the SH1 map is -1500 m, the top contour of the SH2 map is -1540 m, and the top contour of the S2 map is -1600 m. Depth reference is sea level. The model is built using the Convergent Interpolation Algorithm. X–Y increments equal to 10 m. Modelled area is 12×5 km.

we have also simulated 20 years of heat storage in the reservoir, and the results for one realisation are shown in Table 5 and Fig. 16.

Discussion

Based on the presented results we have little doubt that the Gassum Formation as it is found in the Stenlille structure is highly relevant for heat storage in Denmark. Geologically, the sand layers have a high lateral continuity due to their probable origin as amalgamated, up to 30 m thick sandstone bodies deposited in a shallow marine environment. Their shallow marine origin is also reflected in high sorting and consequent excellent reservoir properties with porosities around 25% and permeabilities in the range 1000–10 000 mD. The porosity is comparable to the deep geothermal reservoirs studied by Sip-

pel *et al.* (2013) and Zeghici *et al.* (2015), whereas the permeability of the Gassum Formation sandstone is significantly higher than those of the sandstone in the Berlin area (500 mD, Sippel *et al.* 2013) and the limestones near Bucharest (10 mD, Zeghici *et al.* 2015). The sand layers in Stenlille are interbedded with shale of similar porosity but a permeability around 0.01 mD, so heat transport by advection from the sandstone to shale is negligible. Some heat transport takes place by diffusion: our petrophyscial model indicates that both lithologies have similar thermal conductivities in the range 2.5–3.5 W/(m K), caused by similar porosities and similar mineral thermal properties, although the sandstone is more cemented and has a lower Biot's coefficient (Orlander *et al.* 2018). This is in contrast to earlier estimates where shale is allocated low thermal conductivity (e.g. Møller *et al.* 2019) and is caused by a reinterpretation of the thermal conductivity data for clay published by Brigaud & Vasseur (1989).
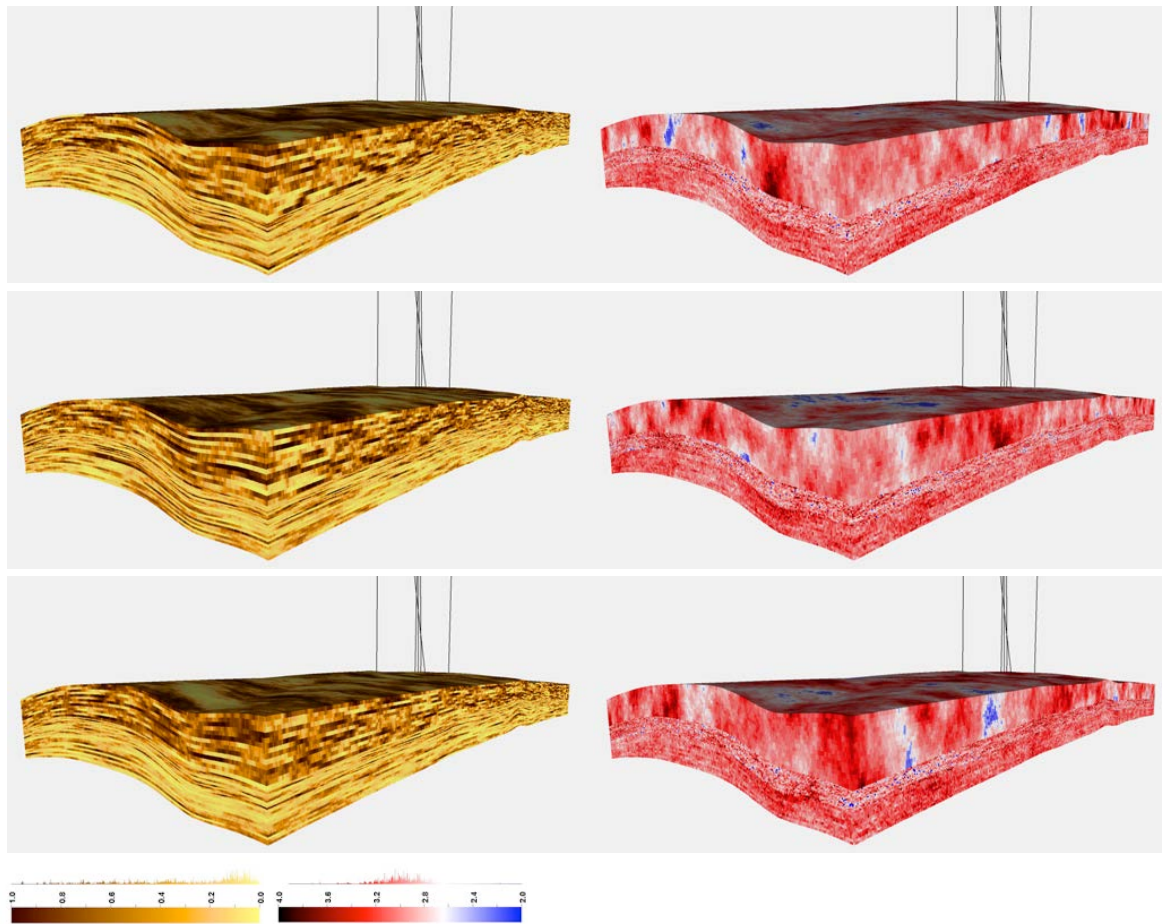
Fig. 13. Three geostatistical realisations for clay fraction (left), with sandstones in yellow and shales in brown, and corresponding thermal conductivity (right), with blue representing low values around 2 W m^{-1}K^{-1} and red representing high values around 4 W m^{-1}K^{-1}. Cell size is 10×10×5 m. For scale, refer to Fig. 12.

The high preserved porosity of the Gassum Formation at Stenlille reflects the modest maximal palaeoburial of *c*. 2 km, based on the interpretation of Japsen & Bidstrup (1999). The reservoir is thus shallow enough to have maintained good reservoir properties, and at the same time the burial is deep enough, so that the consequent reservoir temperature of *c*. 55°C is high enough to diminish heat loss due to convection and low enough to be increased by injection of 75°C hot water.

With respect to the technical characteristics of the hypothetical Stenlille heat storage facility, the results from our finite difference modelling are quite similar to the results of the simplified model by Jeon *et al*. (2015), probably due to the simple geological geometry. The recovery efficiency of 70% after four years is similar, the penetration rate near the well is the same (almost 60 m). A closer look at the equation set for our model indicates that the permeability field has the highest importance for the recovery efficiency. This is also in accordance with the findings in Jeon *et al*. (2015).

The three scenarios simulated for the finite difference model are based on the principle of geostatistics, so that each realisation represents an equally probable representation of the spatial distribution of permeability and thermal conductivity. The variability of the results from the three realisations allows us to evaluate the uncertainty of the estimated recovery efficiencies. For all three realisations we obtain a similar penetration rate of hot water in the near-well region and the same order of magnitude of the recovery efficiency, reflecting a moderate-to-small uncertainty. From Table 3 we notice a drop-off in recovery efficiency of 8% during the simulation of the first cycle and of 7.6% at the fourth cycle. This means that the system can be considered stable after four years of simulation. The same happens if we look at the simulation after 20 years (Fig. 16 and Table 5). The drop-off of the recovery efficiency is again 8%. The system is still stable after 20 years of simulation of an HT-ATES system.
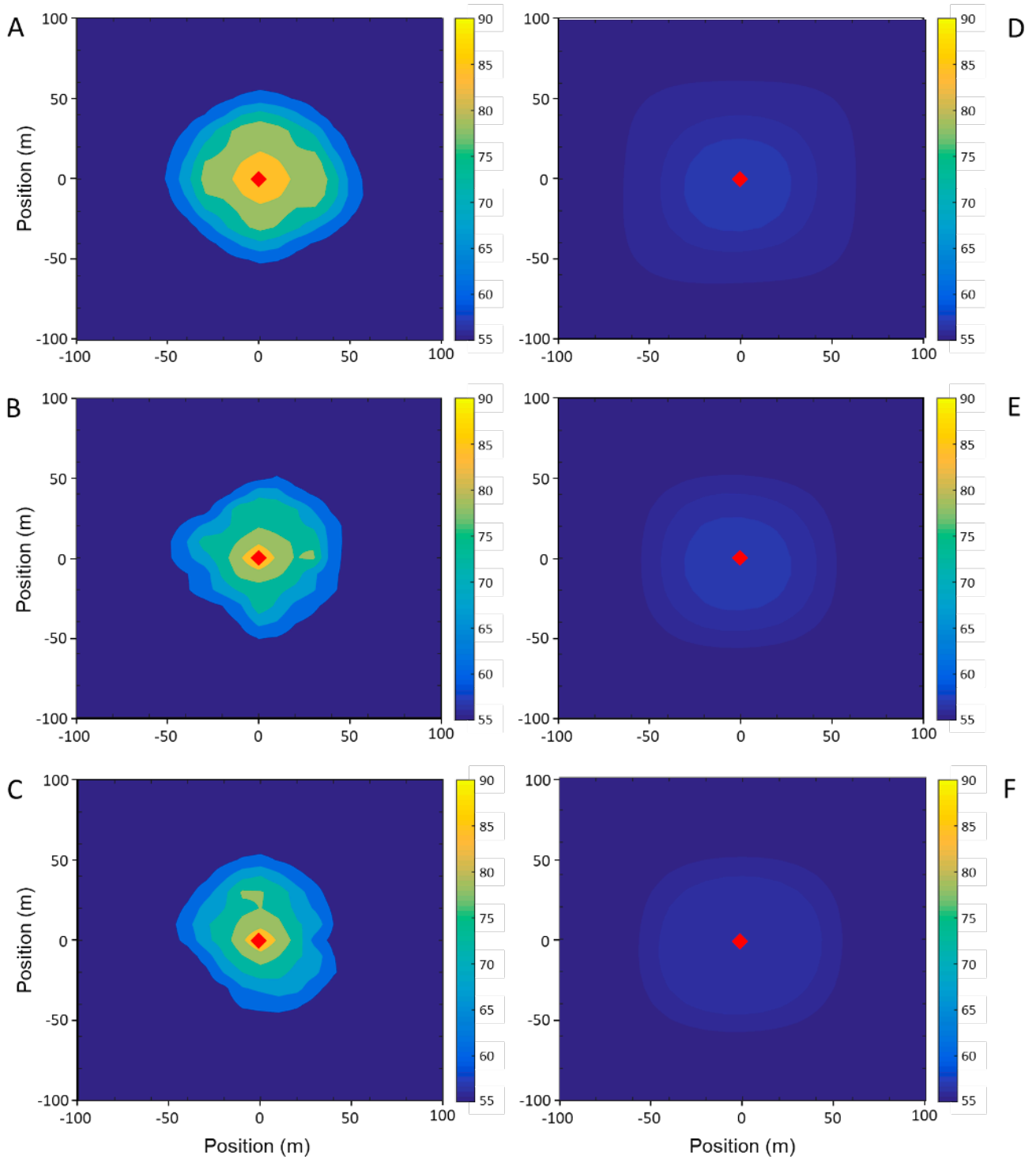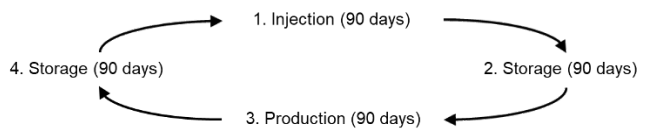
Fig. 14. Three realisations of the temperature field in the Stenlille reservoir after four modelled injection cycles. **A, B, C**: Horizontal sections through the reservoir after injection, **A**: first realisation. **B**: second realisation. **C**: third realisation. **D, E, F**: Horizontal sections through the reservoir after production, **D**: first realisation. **E**: second realisation. **F**: third realisation. Temperatures in °C. The red filled diamond represents the well. At the bottom of the figure, the successive stages in one injection cycle are shown.
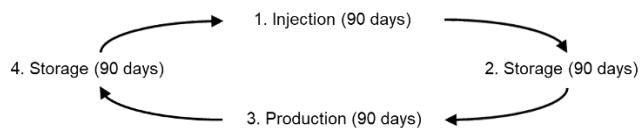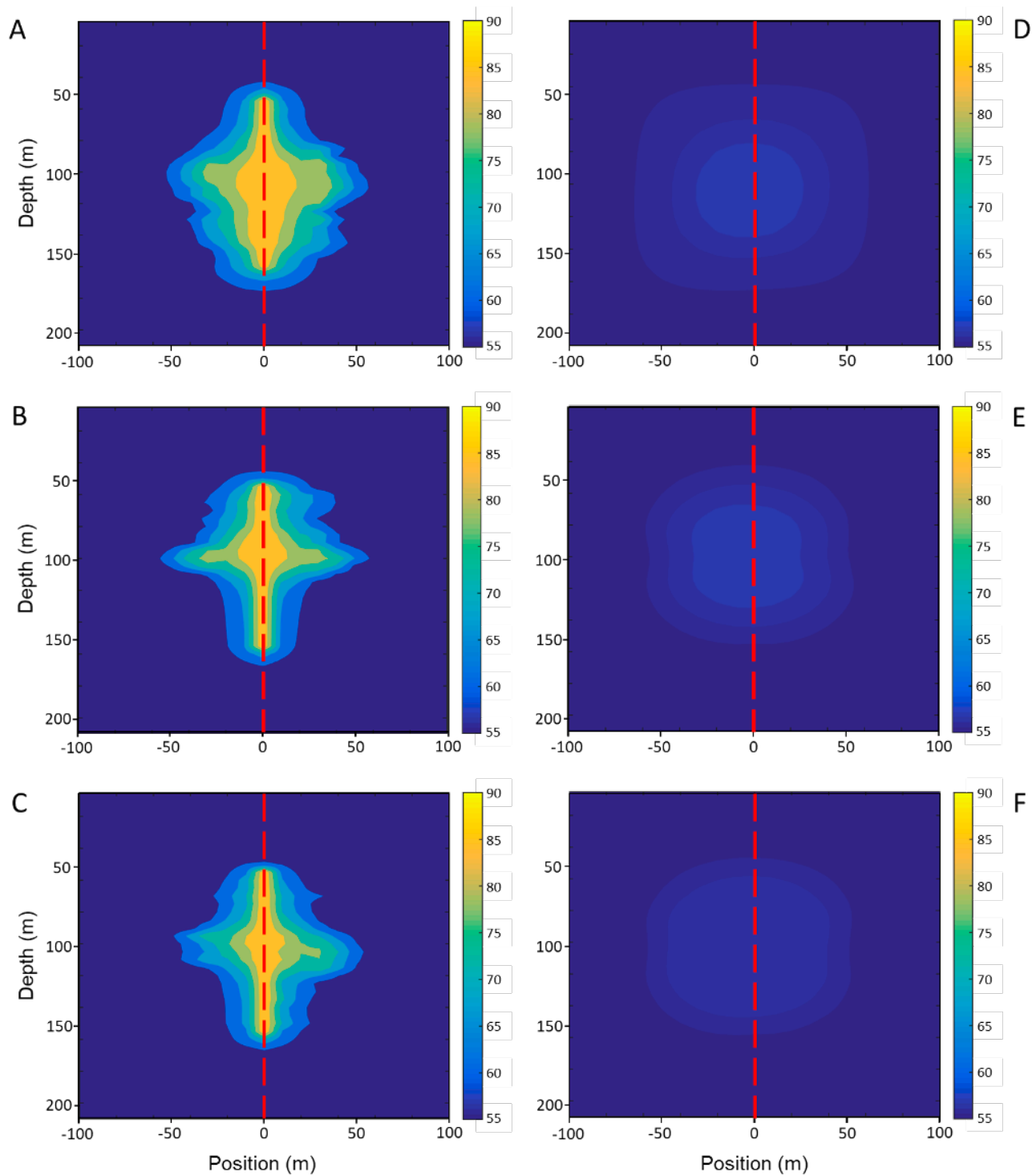
Fig. 15. Three realisations of the temperature field in Stenlille reservoir after four modelled injection cycles. **A, B, C**: Vertical sections through the reservoir after injection, **A**: first realisation. **B**: second realisation. **C**: third realisation. **D, E, F**: Vertical sections through the reservoir after production, **D**: first realisation. **E**: second realisation. **F**: third realisation. Temperatures in °C. The red dashed line represents the well. At the bottom of the figure, the successive stages in one injection cycle are shown.

Table 3. Thermal performances and recovery efficiencies for the Stenlille reservoir

Heat injected (J)	Heat left (J)	Heat stored (J)	Heat recovered (J)	Recovery efficiency (%)	Realization	Cycle
35.7·10¹²	8·10¹²		27.6·10¹²	77.5	1	1
48.3·10¹²	11.7·10¹²	12.6 10¹²	36.6·10¹²	75.8	1	4
24.2·10¹²	6.8·10¹²		17.4·10¹²	71.8	2	1
34.5·10¹²	10.3·10¹²	10.3·10¹²	24.2·10¹²	70.2	2	4
19.9·10¹²	6·10¹²		13.8·10¹²	69.6	3	1
29.1·10¹²	9.2·10¹²	9.2·10¹²	19.9·10¹²	68.2	3	4

Results after one injection cycle of 90 days, one storage cycle of 90 days, one production cycle of 90 days and 90 days of inactivity (cycle 1) and after four injection cycles of 90 days each, four storage cycles of 90 days each, four production cycles of 90 days each and four cycles of inactivity of 90 days each (cycle 4).
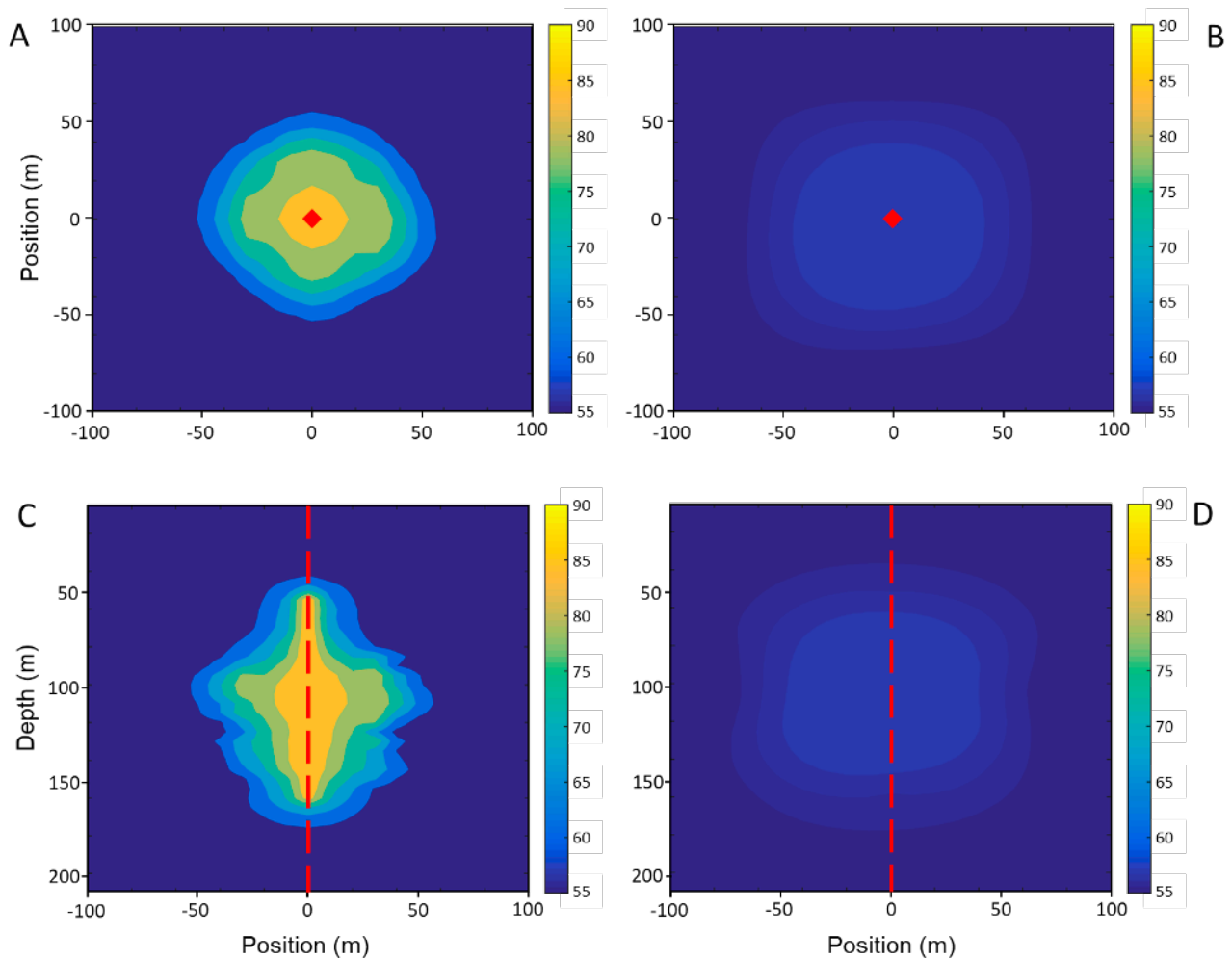

Fig. 16. Temperature field after 20 injection cycles of the first realisation. **A**: Horizontal section through the reservoir after injection. **B**: Horizontal section through the reservoir after production. **C**: Vertical section through the reservoir after injection. **D**: Vertical section through the reservoir after production. The red filled diamond and dashed line represent the well. Temperatures in °C.

Table 4. Modelled recovery efficiency, thermal breakthrough time and storage capacity for the three different realizations of the Stenlille structure

	model
Recovery efficiency (%)	77-72-70 76-70-68
Thermal breakthrough time (years)	66
Storage capacity (J)	1.8·10¹⁸

Table 5. Thermal performances and recovery efficiencies for one realization of the Stenlille reservoir

Heat injected (J)	Heat left (J)	Heat stored (J)	Heat recovered (J)	Recovery efficiency (%)	Realization	Cycle
$35.7 \cdot 10^{12}$	$8 \cdot 10^{12}$		$27.6 \cdot 10^{12}$	77.5	1	1
$53.4 \cdot 10^{12}$	$16.24 \cdot 10^{12}$	$17.7\ 10^{12}$	$37.2 \cdot 10^{12}$	69.6	1	20

Results after one injection cycle of 90 days, one storage cycle of 90 days, one production cycle of 90 days and 90 days of inactivity (cycle 1), and after twenty injection cycles of 90 days each, twenty storage cycles of 90 days each, twenty production cycles of 90 days each and twenty cycles of inactivity of 90 days each (cycle 20).

Conclusions

The Gassum Formation in the Stenlille area is formed by several amalgamated sandstone bodies separated by heterolithic intervals. The sandstone bodies are laterally continuous. We conclude that the Gassum Formation was deposited in a shallow marine environment. These findings are reflected in the high continuity and good reservoir properties of the sandstones.

We found the following characteristic physical properties in Stenlille: The average porosity for sandstone is 25–30%. The average permeability ranges from 1000 mD to 10 000 mD for sandstone and is around 0.01 mD for shale. The average heat capacity was found to be 2–2.5 MJ m^{-3} K^{-1} for shale and 2.5–3 MJ m^{-3} K^{-1} for sandstone, whereas the thermal conductivity was found to be 2.5–3.5 W/(m K) for both lithologies.

Based on three scenarios of a Petrel-based geostatistical model, finite difference reservoir simulation indicates an average recovery efficiency of 72%, a storage capacity of up to 2 10^{18} J and a thermal breakthrough time of 66 years.

All data indicate that an HT-ATES system in the Stenlille structure is feasible.

Acknowledgements

References

Applied Precision Ltd. 2015: Isomet 2114 – User's Guide. Applied Precision Ltd. https://www.manualslib.com/manual/1346306/Applied-Precision-Isomet-2114.html (accessed 30 January 2020).

Archie, G.E. 1942: The Electrical Resistivity Log as an Aid in Determining Some Reservoir Characteristics. Petroleum Transactions of the AIME 146, 54–62. https://doi.org/10.2118/942054-g

Ataer, O.E. 2006: Storage of thermal energy in Energy Storage Systems. In: Gogus, Y. (ed.): Encyclopedia of Life Support Systems (EOLSS), Developed under the Auspices of the UNESCO, Eolss Publishers, Oxford. http://www.eolss.net (30/1 2020)

Biot, M. 1941: General theory of three dimensional consolidation. Journal of Applied Physics 12, 155–164. https://doi.org/10.1063/1.1712886

Brigaud, F. & Vasseur, G. 1989: Mineralogy, porosity and fluid control on thermal conductivity of sedimentary rocks. Geophysical Journal 98, 525–542. https://doi.org/10.1111/j.1365-246x.1989.tb02287.x

Fabricius, I.L. 2014: Burial stress and elastic strain of carbonate rocks. Geophysical Prospecting 62, 1327–1336. https://doi.org/10.1111/1365-2478.12184

Fuchs, S. & Förster, A. 2014: Well-log based prediction of thermal conductivity of sedimentary successions: a case study from the Northern German Basin. Geophysical Journal International 196, 291–311. https://doi.org/10.1093/gji/ggt382

Gassmann, F. 1951: Über die Elastizität poröser Medien. Vierteljahrsschrift der Naturforschenden Gesellschaft in Zürich 96, 1-23.

Gulbrandsen, M.L., Cordua, K.S., Bach, T. & Hansen T.M. 2017: Smart Interpretation – Automatic geological interpretations based on supervised statistical models. Computational Geosciences 21, 427–440. https://doi.org/10.1007/s10596-017-9621-8

Hamberg, L. & Nielsen, L.H. 2000: Shingled, sharp-based shoreface sandstone: depositional response to stepwise forced regression in a shallow basin, Upper Triassic Gassum Formation, Denmark. Geological Society, London, Special Publication 172, 69–89. https://doi.org/10.1144/gsl.sp.2000.172.01.04

Japsen, P. & Bidstrup, T. 1999: Quantification of late Cenozoic erosion in Denmark based on sonic data and basin modelling. Bulletin of the Geological Society of Denmark 46, 79–99.

Jeon, J.S., Lee, S.R., Pasquinelli, L. & Fabricius I.L. 2015: Sensitivity analysis of recovery efficiency in high-temperature aquifer thermal energy storage with single well. Energy 90, 1349–1359. https://doi.org/10.1016/j.energy.2015.06.079

Klinkenberg, L.J. 1941: The permeability of porous media to liquids and gases. In: Drilling and Production Practice, New York, 1 January 1941, API-41-200, 200–218.

Krogstad, S., Lie, K.-A., Møyner, O., Nilsen, H.M., Raynaud, X. & Skaflestad B. 2015: MRST-AD – an open-source framework for rapid prototyping and evaluation of reservoir simulation problems. 2015 SPE Reservoir Simulation Symposium, Houston, Texas, USA, 23–25 February 2015, SPE-173317-MS, 1–26. https://doi.org/10.2118/173317-ms

Kupfersberger, H. 2009: Heat transfer modelling of the Leibnitzer Feld aquifer, Austria. Environmental Earth Sciences

59, 561–571. https://doi.org/10.1007/s12665-009-0054-0

Laier, T. 2012: Results of monitoring groundwater above the natural gas underground storage at Stenlille, Denmark. Geological Survey of Denmark and Greenland Bulletin 26, 45–48.

Lee, J. 1982: Well testing. SPE Textbook Series 1, 159 pp. Richardson, TX: Society of Petroleum Engineers, ISBN: 978-089520-317-5.

Lee, K.S. 2013: Underground thermal energy storage. In: Lee, K.S.: Green Energy and Technology, 15–26. London: Springer Verlag. https://doi: 10.1007/978-1-4471-4273-7

Lerm, S., Westphal, A., Miethling-Graff, R., Alawi, M., Seibt, A., Wolfgramm, M. & Würdemann, H. 2013: Thermal effects on microbial composition and microbiologically induced corrosion and mineral precipitation affecting operation of a geothermal plant in a deep saline aquifer. Extremophiles 17, 311–327. https://doi.org/10.1007/s00792-013-0518-8

Lie, K.-A., Krogstad, S., Ligaarden, I.S., Natvig, J.R., Nilsen, H.M. & Skaflestad, B. 2012: Open source MATLAB implementation of consistent discretisations on complex grids. Computational Geosciences 16, 297–322. https://doi: 10.1007/s10596-011-9244-4

Lie, K.-A. 2015: An introduction to reservoir simulation using MATLAB: User guide for the Matlab Reservoir Simulation Toolbox (MRST), 383 pp. Oslo: SINTEF ICT.

Major, M., Poulsen, S.E. & Balling, N. 2018: A numerical investigation of combined heat storage and extraction in deep geothermal reservoirs. Geothermal Energy 6, 16 pp. https://doi.org/10.1186/s40517-018-0089-0

Mathiesen, A., Kristensen, L., Nielsen, C.M., Weibel, R., Hjuler, M.L., Røgen. B., Mahler, A. & Nielsen L.H. 2013: Assessment of sedimentary geothermal aquifer parameters in Denmark with focus on transmissivity. European Geothermal Congress 2013, Pisa, Italy, 3–7 June 2013, 9 pp.

Mavko, G., Mukerji, T. & Dvorkin, J. 1998: The rock physics handbook. Tools for seismic analysis of porous media, 339–342. Cambridge University Press, Cambridge.

Mbia, E., Fabricius, I.L., Frykman, P., Krogsbøll, A. & Dalhoff, F. 2014: Permeability, compressibility and porosity of Jurassic shale from the Norwegian-Danish Basin. Petroleum Geoscience 20, 257–281. https://doi.org/10.1144/petgeo2013-035

Mortensen, J., Engstrøm, F. & Lind, I.L. 1998: The relation among porosity, permeability and specific surface of chalk from the Gorm Field, Danish North Sea. SPE Reservoir Evaluation and Engineering 1, 245–251. https://doi.org/10.2118/31062-pa

Møller, I., Balling, N. & Ditlevsen, C. 2019: Shallow subsurface thermal structure onshore Denmark: temperature, thermal conductivity and heat flow. Bulletin of Geological Society of Denmark 67, 29–52.

Nielsen, L.H. 2003: Late Triassic-Jurassic development of the Danish Basin and the Fennoscandian Border Zone, southern Scandinavia. Geological Survey of Denmark and Greenland Bulletin 1, 459–526.

Nielsen, L.H., Mathiesen, A. & Bidstrup, T. 2004: Geothermal energy in Denmark. Geological Survey of Denmark and Greenland Bulletin 4, 17–20.

Orlander, T., Adamopoulou, E., Asmussen, J.J., Marczyński, A.A., Milsch, H., Pasquinelli, L. & Fabricius, I.L. 2018: Thermal conductivity of sedimentary rocks using Biot's coefficient and other well log derived parameters. Geophysics 83, D173–D185. https://doi.org/10.1190/geo2017-0551.1

Peaceman, D.W. 1991: Fundamentals of Numerical Reservoir Simulation, 175 pp. Elsevier, New York. ISBN 0444415785.

Pedersen, A.S., Elmegaard, B., Christensen, C.H., Kjøller, C., Elefsen, F., Hansen, J.B., Hvid, J, Sørensen, P.A., Kær, S.K., Vangkilde-Pedersen, T. & Jensen, T.F. 2014: Status and recommendations for RD&D on energy storage technologies in a Danish context. Report, Technical University of Denmark, 136 pp. https://backend.orbit.dtu.dk/ws/portalfiles/portal/103523196/Status_and_recommendations_for_RD.pdf (accessed 31 January 2020).

Petrel, 2015: Shared earth – critical insight, Petrel E&P software platform user manual. Schlumberger. https://www.software.slb.com/products/petrel

Poulsen, S., Balling, N. & Nielsen, S.B. 2015: A parametric study of the thermal recharge of low enthalpy geothermal reservoirs. Geothermics 53, 464–478. https://doi.org/10.1016/j.geothermics.2014.08.003

Robertson, E.C. 1988: Thermal properties of rocks. United States Geological Survey, Open-File-Report 88-441, 106 pp. https://doi.org/10.3133/ofr88441

Rosenbrand, E., Haugwitz, C., Jacobsen, P.S.M., Kjøller, C. & Fabricius, I.L. 2014: The effect of hot water injection on sandstone permeability. Geothermics 50, 155–166. https://doi.org/10.1016/j.geothermics.2013.09.006

Saeid, S., Al-Khoury, R. & Barends, F. 2013: An efficient computational model for deep low enthalpy geothermal systems. Computers and Geoscience 51, 400–409. https://doi.org/10.1016/j.cageo.2012.08.019

Saeid, S., Al-Khoury, R., Nick H.M. & Barends, F. 2014: Experimental-numerical study of heat flow in deep low-enthalpy geothermal conditions. Renewable Energy 62, 716–730. https://doi.org/10.1016/j.renene.2013.08.037

Schärli, U. & Rybach, L. 2001: Determination of specific heat capacity on rock fragments. Geothermics 30, 93–110. https://doi.org/10.1016/s0375-6505(00)00035-3

Schout, G., Drijver, B., Gutierrez-Neri, M. & Schotting, R. 2014: Analysis of recovery efficiency in high-temperature aquifer thermal energy storage: a Rayleigh-based method. Hydrogeology Journal 22, 281–291. https://doi.org/10.1007/s10040-013-1050-8

Sippel, J., Fuchs, S. & Cacace, M. 2013: Deep 3D thermal modelling for the city of Berlin (Germany). Environmental Earth Sciences 70, 3545–3566. https://doi.org/10.1007/s12665-013-2679-2

Tanikawa, W. & Shimamoto, T. 2009: Comparison of Klinkenberg-corrected gas porosity and water permeability in sedimentary rocks. International Journal of Rock mechanics and Mining science 46, 229–238.

Turcotte, D. & Schubert, G. 2014: Geodynamics, Third Edition, 160–228, 263–334, 425–463. Cambridge University Press, Cambridge. https://doi.org/10.1017/cbo9780511843877

Vejbæk, O.V. 1989: Effects of asthenospheric heat flow in basin modelling exemplified with the Danish Basin. Earth and Planetary Science Letters 95, 97–114. https://doi.org/10.1016/0012-821x(89)90170-2

Visser, P.W., Kooi, H. & Stuyfzand, P.J. 2015: The thermal impact of aquifer thermal energy storage (ATES) systems: a case study in the Netherlands, combining monitoring and modeling. Hydrogeology 23, 507–532. https://doi.org/10.1007/s10040-014-1224-z

Zeghici, R.M., Essink G.O., Hartog, N. & Sommer, W. 2015: Integrated assessment of variable density–viscosity groundwater flow for a high temperature mono-well aquifer

thermal energy storage (HT-ATES) system in a geothermal reservoir. Geothermics 55, 58–68. https://doi.org/10.1016/j.geothermics.2014.12.006

Ziegler, P.A. 2005: Europe: Permian to recent evolution. In: Selley, R.C., Cocks, L.R.M. & Plimer, I.R. (eds), Encyclopedia of Geology, 102–125. Elsevier, Amsterdam. https://doi.org/10.1016/b0-12-369396-9/00469-x